RSC Advances

RSC Advances

ARTICLE

Electrocatalytic Properties of Iron Chalcogenides as Low-Cost Counter Electrode Materials for Dye-sensitized Solar Cells

Jiahao Guo,‡[a,b] Suxia Liang,‡[a] Yantao Shi,[a,]*Ce Hao,[a] Xuchun Wang,[b] and Tingli Ma[c,d]*

Developing cost-effective and highly electrocatalytic Pt-free counter electrode (CE) materials for triiodide reduction has become a major interest for dye-sensitized solar cells (DSCs). In a heterogeneous catalytic system, iron chalcogenides like FeS_2 and $FeSe_2$ have demonstrated excellent catalytic activity when serving as CE materials in DSCs. However, theoretical and experimental studies have yet to be conducted to investigate the catalytic activity of iron chalcogenides in energy conversion and storage devices under same condition. In this work, FeS_2, $FeSe_2$, and $FeTe_2$ were selected as our research object to systematically investigate and compare the regulatory mechanisms of the changes in the catalytic activity of iron chalcogenides. Theoretical research reveals that the iodine adsorption and charge exchange of these three materials occurred efficiently in heterogeneous catalytic systems. Experimental results further show that these three materials exhibited excellent catalytic activities. The conversion efficiencies of the corresponding DSCs are comparable to those of the sputtered Pt CE. This study also provides a method to rationally screen cost-effective and highly efficient catalytic materials for electrocatalysis applications.

1. Introduction

Increasing energy demands have prompted researchers to exploit highly efficient, cost-effective, and environmentally friendly alternative energy conversion and storage devices.[1] As a type of photovoltaic device that directly converts sunlight into electrical energy, dye-sensitized solar cells (DSCs) can satisfy these requirements; as such, DSCs have been intensively investigated.[2–4] Typical DSCs are composed of a dye-sensitized mesoporous oxide layer (TiO_2), an electrolyte containing an iodide/triiodide (I_3^-/I^-) redox couple, and a counter electrode (CE) that regenerates reduced species in electrolytes.[5] Figure 1 shows the working principle of DSCs.

A superior CE material generally exhibits high electrocatalytic activity, good electrical conductivity, and chemical stability to

Figure 1. Working principle of a dye-sensitized solar cell

collect photogenerated electrons from an external circuit and reduce I_3^- into I^- for subsequent dye regeneration.[6] Therefore, Pt-based CEs prepared by either sputtering or pyrolysis have been widely used to fabricate DSCs. However, Pt-based CEs are usually characterized by various limiting factors including high cost, element scarcity, and decreased activity derived from serious corrosion cause by iodine species from an electrolyte solution; these factors likely impede the scalable applications of DSCs.[7] Hence, cost-effective and highly electrocatalytic alternative CE materials should be developed.[8–22]

Iron (Fe) widely exists in the Earth's crust and ranks fourth among the most abundant elements, following oxygen, silicon, and aluminum. Fe compounds with various compositions, valence states, and crystal structures[23,24] are abundant, cost effective, and environmentally friendly; furthermore, Fe compounds have been extensively investigated because of important optical, electrical, optoelectronic, and transport properties.[25-31] Some Fe compounds that exhibit excellent catalytic activity and stability can also serve as electrocatalysts (for oxygen reduction reaction) in fuel cells and other kinds of electrochemical cells.[32,33] Other Fe compounds are efficient electrocatalysts as CEs for DSCs. For example, Wang et al.[34] reported that DSCs with FeS_2 nanocrystal-based CE exhibit a power conversion efficiency (*PCE*) of 7.31%. Yang et al.[35] confirmed theoretically and experimentally that α-Fe_2O_3 nanocrystal is an excellent CE candidate with high electrocatalytic activity for I_3^-
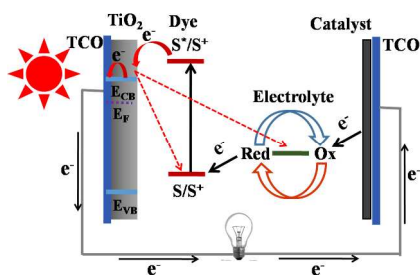
reduction. Our group[36] further reported a composite catalyst (biomass carbon and Fe_3O_4) as a CE material for DSCs; using this composite catalyst, we obtained a high *PCE* of 8.11% in DSCs. We simultaneously introduced hierarchical Fe_3O_4 structures to DSCs as a CE with a *PCE* of 7.65%.[37] In a heterogeneous catalytic system, iron chalcogenides have demonstrated excellent catalytic activity. As cathode catalysts, CE materials exhibit a catalytic activity greatly influenced by the outer electronic structure and surface morphological characteristics of electrode materials in a heterogeneous catalytic reaction.[34]

This study is the first to systematically illustrate the high catalytic activity of iron chalcogenides by using theoretical and experimental methods. We selected three iron chalcogenides FeS_2, $FeSe_2$, and $FeTe_2$ as our research object from the outer electron of a nonmetallic element changes periodically. We initially calculated the iodine adsorption and charge exchange of the three iron chalcogenides on the basis of the density functional theory (DFT) theory; we found that these chalcogenides exhibit excellent catalytic activities in I_3^- reduction. We then synthesized FeS_2 and $FeSe_2$ by using a similar reductant-free solvothermal method. We also synthesized $FeTe_2$ by using a solvent thermal method. Our experimental results further showed that these three samples exhibited excellent catalytic activities as CE materials involved in I_3^- reduction. DSCs based on these three CE materials also exhibited photoelectric properties comparable to DSCs based on Pt CE. Our research confirmed that iron chalcogenides are good electrocatalytic cathode materials. Therefore, these materials can be used to enhance the applications of iron chalcogenides.

2. Computational Method

DFT computations were performed using projector augmented wave (PAW) potentials and Perdew−Burke−Ernerhof (PBE) functional implemented in Vienna ab initio simulation package (VASP).[38-41] Relaxations were carried out using a conjugate-gradient algorithm. The selected energy convergence was 1×10^{-5} eV/atom, and relaxations were terminated if all of the forces were $<$ 0.01eV/Å. The cutoff energy was set as 364 eV for FeS_2 and 347 eV for $FeSe_2$ and $FeTe_2$. The Brillouin zone was integrated using Monkhorst−Pack-generated sets of k points. We applied $15 \times 15 \times 15$, $11 \times 11 \times 11$, and $9 \times 9 \times 9$ k-point meshes for FeS_2, $FeSe_2$, and $FeTe_2$ in bulk computations, respectively. The occupancy of one-electron states was calculated using Gaussian smearing (SIGMA = 0.1 eV). The primitive cell of the three iron chalcogenides was used when the band structure was calculated.

Surface computations were performed using a slab model. A typical low index surface (111) was considered in this study. FeS_2 (111), $FeSe_2$ (111), and $FeTe_2$ (111) surfaces were modeled as a p (1 $\times$ 1) periodic slab; the vacuum between slabs was 20 Å. The atoms in the two bottom layers were fixed, and all other atoms were fully relaxed. A corresponding $3 \times 3 \times 1$ k-point mesh was applied during optimization.

3. Experimental

3.1 Material preparation

Pyrite FeS_2 sample

A mixture of 0.5 mmol Fe_2O_3, 10 mmol sulphur powder, 70% oleylamine (OLA, 20 ml), 90% Oleic acid (OA, 2 ml), and 0.2 mmol hexadecyltrimethyl ammonium bromide (CTAB) was added to a 100 ml three-necked flask. The mixture was heated at a rate of 25 °C·min^{-1} from room temperature to 290 °C, kept for 1 h under magnetic stirring, and cooled to room temperature. The sample was washed with ethanol to remove the excess surfactants and solvents. The precipitate was dried in vacuum at 60 °C overnight.

Orthorhombic $FeSe_2$ sample

The $FeSe_2$ samples were synthesized by mixing 2mmol Se powder, 1 mmol $Fe(OH)_3$, and 10 ml of OLA in a 100 ml three-necked flask. The reaction temperature was 200 °C, and the other procedures are the same as those in the FeS_2 sample preparation.

Orthorhombic $FeTe_2$ sample

$FeTe_2$ was prepared by a solvothermal method. Ethylenediamine was placed in a 100ml Teflon liner autoclave until 80% of the volume was filled. Afterward, 2 mmol Te powder and 1 mmol $FeCl_2·4H_2O$ were added to the autoclave. The autoclave was sealed and maintained at 180 °C. After the reaction was completed, the autoclave was allowed to cool naturally to room temperature. The precipitate was centrifuged and washed with distilled water and absolute ethanol several times to remove by-products and impurities. The product was dried in vacuum at 60 °C overnight.

3.2 Preparation of chalcogenides CEs and cell fabrication

FeS_2, $FeSe_2$, and $FeTe_2$ CEs were prepared. In brief, 200mg of FeS_2, $FeSe_2$, or $FeTe_2$ powder and 4 g of ZrO_2 pearl were dispersed in 4 ml isopropanol and milled for 4 h. The prepared chalcogenide slurry was sprayed onto an FTO glass (Asahi Glass, type-U, 14 U sq^{-1}, Japan) with an airbrush (TD-128, Tiandi Co., Ltd.) connected to a mini compressor. The FTO substrate coated with an FeS_2, $FeSe_2$, or $FeTe_2$ film was then annealed under a N_2 atmosphere at 500 °C for 30 min in a tube furnace to obtain the expected FeS_2, $FeSe_2$, or $FeTe_2$ CEs. The Pt CE was prepared in according with our previous work.[42]

A TiO_2 film (P25, Degussa, Germany) photoanode was fabricated via a screen-printing technique on the FTO conductive glass in accordance with previously described methods.[43] The TiO_2 film was immersed in a 5×10^{-4} M acetonitrile/tert-butyl alcohol (1:1 volume ratio) solution of cis-bis (isothiocyanato) bis(2,2'-bipyridyl-4−4'-dicarboxylato)-ruthenium (II) bis-tetrabutylammonium dye(N719, Solaronix SA, Switzerland; Figure 2) at room temperature for 21 h to absorb the dye. The TiO_2 photoanodes were then removed from the solution, rinsed with ethanol to remove the excess adsorbed dye, and dried in air at room temperature. A DSCs device was fabricated by placing the chalcogenide CEs on the N719 dye-sensitized TiO_2 photoelectrode and clipped as an open cell for measurements. The DSCs device was then filled with the redox electrolyte composed of 0.06 M LiI, 0.6 M 1-butyl-3-methylimidazolium iodide, 0.03 M I_2, 0.5 M 4-tert-butyl pyridine, and 0.1 M guanidiniumthiocyanate in acetonitrile solution via capillary force. The as-assembled DSCs with an active area of 0.16 cm^2 were subjected to photovoltaic performance tests. A symmetrical cell was assembled by sandwiching two identical CEs with the same electrolyte as used in
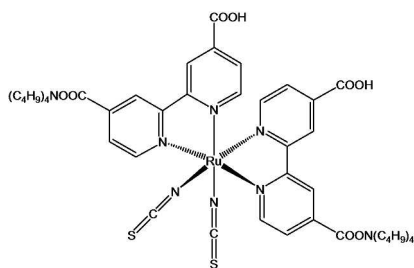
Figure 2. Structure diagram of N719 dye

the DSCs assembly. The as-assembled symmetrical cell was then subjected to electrochemical impedance spectroscopy and Tafel polarization measurement.

3.3 Characterizations of CE materials and DSCs

The X-ray powder diffraction (XRD) profiles of the as prepared samples were measured using an X-ray powder diffractometer (D/Max 2400, Rigaku, Japan) with Cu Kα radiation (λ = 0.154 nm). The surface morphological characteristics and microstructure of the chalcogenide samples were examined through field emission scanning electron microscopy (FEI HITACHI S-4800). Cyclic voltammetry (CV) was performed using a CHI630D electrochemical workstation (Chenhua, Shanghai) in a three-electrode system of an anhydrous acetonitrile solution containing 0.1 M $LiClO_4$, 10 mM LiI, and 1 mM I_2 at a scan rate of 10 mV s^{-1}. The as-prepared chalcogenide CEs was assigned as a working electrode; a Pt wire was utilized as a counter electrode; an Ag/AgCl electrode was used as a reference electrode. Electrochemical impedance spectroscopy (EIS) measurements were conducted using the symmetrical cell on a computer-controlled electrochemical workstation (Zennium Zahner, Germany) under dark conditions. The geometric active area of the symmetrical cell was 0.64 cm^2. The samples were scanned from 0.1 Hz to 1 MHz with a bias of −0.75 V; the AC amplitude was 10 mV. The obtained EIS data were analyzed using commercially available Z-view software and fitted in terms of an appropriate equivalent electric circuit. Tafel polarization experiments were conducted in an electrochemical workstation (CHI630D, Chenhua, Shanghai) with the symmetrical cell at a scan rate of 10 mV·s^{-1}. The photovoltaic performances of the DSCs were evaluated by a digital source meter (Keithley 2601, computer-controlled, USA) under simulated sunlight illumination condition, which was produced by a solar simulator (PEC-L15, Peccell, Japan). The light power density was calibrated against a Si-based reference cell to accurately simulate the full-sun intensity (100 mW cm^{-2}).
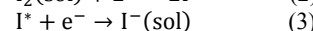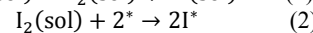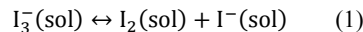
4. Results and discussion

4.1 Theoretical investigation

The DFT computations were performed using PAW potentials and PBE functional implemented in VASP to investigate the electrocatalytic activity of the three iron chalcogenides. We obtained a crystal lattice with parameter values through the full relaxation of atomic positions and lattice constants (Table S1). Our theoretical results are consistent with the experimental values. The electrical conductivity of the CE materials is a critical factor that influences the catalytic activity of CEs in DSCs. To analyze the electronic properties, we determined the band structures of the three iron chalcogenides. The theoretical band gaps of FeS_2, $FeSe_2$, and $FeTe_2$

are 0.55, 0.37, and 0.19eV, respectively, which are consistent with those of Takashi.[44] The results show that these chalcogenides are semiconductors with a small band gap and enhances electrical conductivity, which are essential for CE materials.

On the interface of the CE/electrolyte, the main process is the reduction of electron acceptors from the electrolyte; this process can be expressed as follows: I_3^- (sol) + 2e^- →3I^- (sol); the general consensus of the reaction mechanism can be described as follows:[35]

$$I_3^-(\text{sol}) \leftrightarrow I_2(\text{sol}) + I^-(\text{sol}) \qquad (1)$$
$$I_2(\text{sol}) + 2^* \rightarrow 2I^* \qquad (2)$$
$$I^* + e^- \rightarrow I^-(\text{sol}) \qquad (3)$$

where * represents the free site on the electrode surface and sol refers to acetonitrile solution. The first step occurs rapidly and exhibits equilibrium.[45] The second step involves the dissociation of I_2 into two surface I atoms (I^*) on the electrode surface. The third step shows the removal of I^* to produce the solvated I^- (sol). Therefore, the larger adsorption energy of I on the CE materials can cause the dissociation of I_2 in the second step; the lower work function of the CE materials indicates an efficient electron transfer from the CE to the electrolyte, and this condition is favorable for the third step. On the basis of this consideration, we use the same (111) surface; Fe and chalcogen atom-terminated surfaces were used as a computational model. The adsorption energy of I on iron chalcogenide (111) surfaces and the work function of FeS_2, $FeSe_2$, and $FeTe_2$ (111) surfaces were compared (Table 1). The adsorption energy of I (E_{ad}^I) is defined as follows:[35]

$$E_{ad}^I = E(\text{interface}) + \frac{E(I_2)}{2} - E(I/\text{interface}) \qquad (4)$$

where E(interface), $E(I_2)$, and E(I/interface) are the energies of the interface, I_2, and I adsorbed on the interface in the gas phase,

c
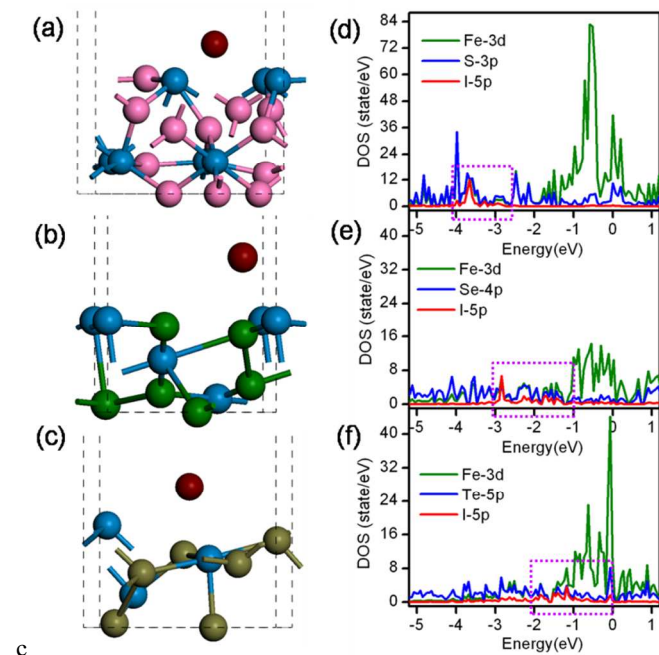
Figure3. Side views of I adsorption on (a) FeS_2 (111), (b) $FeSe_2$ (111), and (c) $FeTe_2$ (111) surfaces; projected density of states (PDOS) of I adsorption on (d) FeS_2 (111), (e) $FeSe_2$ (111), and (f) $FeTe_2$ (111) surfaces. Fermi energy is set as 0 eV. Key: steel cyca, Fe; pink, S; green, Se; olive green, Te; and darkred, I.

**Table 1** Adsorption energy of I (E_{ad}^I) and the work function (Φ) of the three iron chalcogenides.

	FeS$_2$(111)	FeSe$_2$(111)	FeTe$_2$(111)
E$_0$/ev	3.59	1.89	2.54
E$_f$/ev	-2.13	-2.91	-2.14
Φ/ev	5.72	4.80	4.68
E$^I_{ad}$/eV	1.89	1.54	1.04

respectively. Each individual energy term on the right side can be achieved directly through the DFT calculation. Figure 3 shows the optimized structure of FeS$_2$ (111), FeSe$_2$ (111), and FeTe$_2$ (111) surfaces with an I atom and the corresponding projected density of states (PDOS). The calculated adsorption energies of I on FeS$_2$ (111), FeSe$_2$ (111), and FeTe$_2$ (111) surfaces were 1.89, 1.54, and 1.04 eV, respectively (Table 1). On the basis of the PDOS diagram, we found a very strong hybridization between iodine p orbital, iron d orbital, and chalcogen p orbital in the contour plot of the corresponding bonding state. The PDOS images suggest that I $5p$, Fe $3d$, and S $3p$ states hybridize well between −4 and −2.5 eV. This finding indicates that an orbital overlap occurs between I $5p$, Fe $3d$, and S $3p$ electrons; furthermore, this overlap is accounted for the relatively large binding energy of I atom adsorbed on the FeS$_2$ (111) surfaces. On FeSe$_2$ (111) surfaces, I $5p$ orbital interacts with Fe $3d$ and Se $4p$ orbitals between −3 and −1eV. On the FeTe$_2$ (111) surfaces, the orbital overlap region of I $5p$, Fe $3d$, and Te $5p$ states ranges from −2 eV to 0 eV. The locations of the orbital overlap of I with Fe, S, Se, and Te move gradually to Fermi level. This result may be accounted for the decreased adsorption of the I atom on FeS$_2$ (111), FeSe$_2$ (111), and FeTe$_2$ (111) surfaces and for the increased interfacial charge transfer ability.

According to electronic catalysis theory on semiconductors, the catalytic activity of semiconductors is associated with conductivity and work function.[46] To further understand interfacial charge transfer properties, we considered work function in our calculations. Work function (Φ) is equal to vacuum level (E_0) minus Fermi level (E_f). The calculated work function of the FeS$_2$, FeSe$_2$, and FeTe$_2$ (111) surfaces were 5.72, 4.80, and 4.68 eV, respectively. Based on the calculated results, our conclusion is that FeS$_2$ yields a higher adsorption energy of I, and FeTe$_2$ exhibits a lower work function; therefore, the FeS$_2$ (111) surfaces are more beneficial for I$_2$ dissociation, and the FeTe$_2$ CE shows a more efficient electron transfer ability than the other CEs. Considering work function and adsorption energy, we found that three iron chalcogenides exhibit excellent catalytic activities for I$_3^-$ reduction.

4.2 Morphological and structural characterizations of the materials

The crystallinity of CE materials affects the performance of DSCs. The crystallinity and structural data of the obtained iron chalcogenides were collected through XRD. Our results showed that the peaks of FeS$_2$ can be indexed to diffractions from (111), (200), (210), (211), (220), (311), (222), (023), and (231) planes (Figure 4). These findings are consistent with those of a standard FeS$_2$ pyrite (PDF # 42-1340); the characteristic peaks of other impurities were not found. The results also indicate that the obtained FeS$_2$ exhibits a
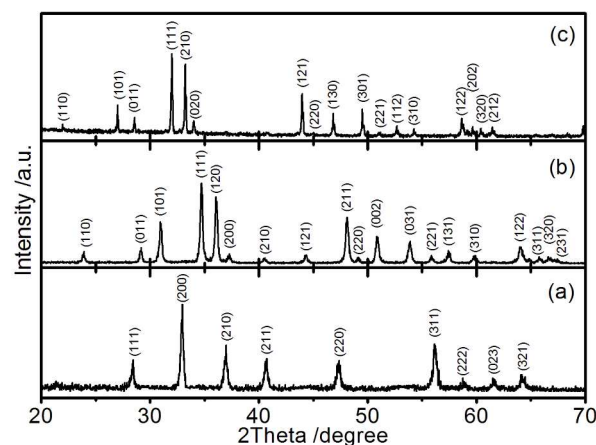
Figure 4. XRD patterns of the as-synthesized (a) FeS$_2$, (b) FeSe$_2$, and (c) FeTe$_2$.

well-crystallized pyrite structure. For FeSe$_2$, the diffraction peaks at 24.04, 29.28, 31.04, 34.72, 36.22, 37.38, 40.68, 44.40, 48.19, 49.24, 50.92, 53.90, 55.91, 57.48, 59.91, 64.09, 65.86, 66.68, and 67.53 can be assigned to (110), (011), (101), (111), (120), (200), (210), (121), (211), (220), (002), (031), (221), (131), (310), (122), (311), (320), and (231) crystal planes, respectively. These diffraction peaks match well with a typical orthorhombic FeSe$_2$ (PDF # 65-2570). In this study, FeTe$_2$ was prepared with a solvothermal method; in this method, ethylenediamine, FeCl$_2$, and Te powder were used as a solvent, an iron source, and a tellurium source, respectively. The products collected in different stages were examined through XRD (Figure S1). Using this approach, we found that theFeTe$_2$ formation is relatively slow because the characteristic peaks of Te in the XRD patterns completely disappeared after 96 h. All of the diffraction peaks of the product collected at 96 h are consistent with those of a typical orthorhombic FeTe$_2$ (PDF # 51-1158); the characteristic peaks of other impurities, such as Te were not detected. The lattice parameters of the three iron chalcogenides are listed in Table S1; these results are in agreement with those of previous studies.[47.48]

The three iron chalcogenides were analyzed through scanning electron microscopy (Figure5). The result showed that the products of FeS$_2$ are in the form of either dispersed nanosized particles or aggregates (Figures5a and 5d). The sizes of nanoparticles ranged from 60 nm to 350 nm. In contrast to FeS$_2$, FeSe$_2$ shows an irregular and hierarchical flower-like structure consisting of nanorods with
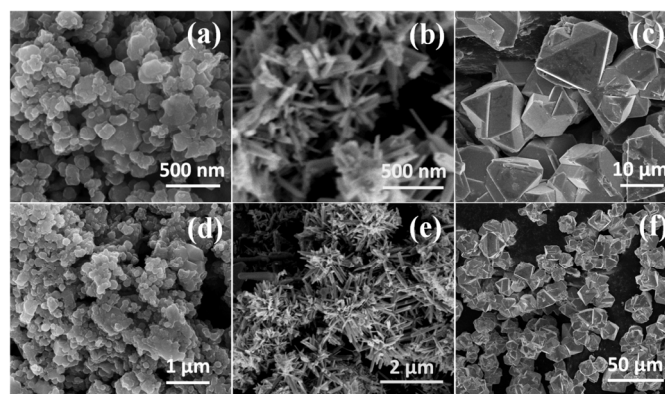
Figure 5. High- andlow-magnification SEM images of FeS$_2$ (a and d), FeSe$_2$ (b and e), and FeTe$_2$ (c and f).

Table 2 EIS, CV, Tafel parameters and photovoltaic performanceof the DSCs based on the three chalcogenides and Pt CE

CEs	$R_s/\Omega cm^2$	$R_{ct}/\Omega cm^2$	CPE/μF	$Z_N/\Omega cm^2$	E_{pp}/mV	$J_0/mAcm^{-2}$	V_{OC}/mV	$J_{SC}/mAcm^{-2}$	FF	PCE/%
Pt	8.27	0.64	42.2	0.45	143	5.82	747	15.28	0.67	7.70
FeS$_2$	8.91	0.44	96.1	2.35	138	6.31	753	15.55	0.68	8.00
FeSe$_2$	8.65	0.55	208.3	0.69	151	5.72	769	14.23	0.72	7.92
FeTe$_2$	7.51	1.08	61.9	9.92	199	4.21	716	15.34	0.66	7.21

a diameter and length of approximately 30 and 300 nm (Figures 5b and 5e). The FeTe$_2$ sample is characterized by irregular and micron-sized polyhedrons (Figures 2c and 2f). The evolution of the morphological characteristic of FeTe$_2$ is shown in Figure S2 and the details have been listed in the Supporting Information. Large particles usually cause a decrease in catalytic active sites; large particles may also affect the catalytic activity of FeTe$_2$.

4.3 Electrocatalytic activity characterization of CEs

CV was performed in acetonitrile solution containing 10 mM LiI, 1 mM I$_2$, and 0.1 M LiClO$_4$ at a scanning rate of 10 mV·s^{-1} to evaluate the electrochemical catalytic activities of the three chalcogenide CEs and Pt CEs for I$_3^-$ reduction in an I$^-$/I$_3^-$ redox shuttle used in DSCs. Figure 6 shows the CV curves of FeS$_2$, FeSe$_2$, FeTe$_2$, and Pt-CE. Each electrode exhibits two typical pairs of oxidation/reduction peaks. The left pair in the CV plots corresponds to I$_3^-$+2e$^-$→3I$^-$; the right pair corresponds to 3I$_2$+2e$^-$→2I$_3^-$. We focused on the characteristics of the left pair because the catalytic activity of a CE is related to the I$_3^-$/I$^-$ redox pair. On the basis of the reaction of I$_3^-$/I$^-$, we found that the cathodic peak current density (J_{pc1}) and the anodic peak current density (J_{pa1}) correspond to I$_3^-$ reduction and I$^-$ oxidation, respectively. The peak separation between anodic and cathodic peaks (E_{pp}) is negatively correlated with the standard electrochemical rate constant of a redox reaction. J_{pc1} and E_{pp} are two critical parameters considered to compare electrocatalytic activities of different CEs. A higher reduction J_{pc1} and a lower E_{pp} indicate a higher catalytic activity.[19]

The CV profiles of the three chalcogenide CEs are similar to those of Pt-CE (Figure 6); this result indicated that the three CEs exhibit abilities similar to Pt-CE in catalyzing the reduction of I$_3^-$ to I$^-$. J_{pc1} of FeS$_2$ and FeSe$_2$ is slightly higher than that of Pt-CE; the cathodic peak potentials of the three CEs are also similar to those of Pt-CE;
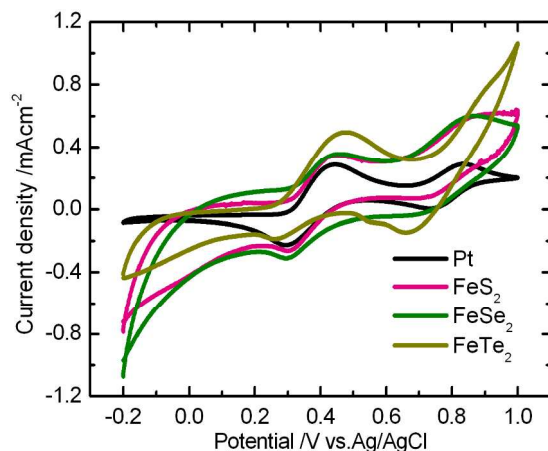
Figure 6. Cyclic voltammograms of the triiodide/iodide redox couple of the three chalcogenideCEs and Pt CEs.

this finding indicated that I$_3^-$ can be reduced more easily on FeS$_2$ and FeSe$_2$ CEs than on Pt-CE. By contrast, these two parameters are generally lower in FeTe$_2$ CE than in Pt-CE; this finding corresponded to a slightly inferior catalytic activity. The relatively lower J_{pc1} of FeTe$_2$ can be attributed to insufficient surface area because of micron-sized particles. E_{pp} of FeS$_2$ and FeSe$_2$ CEs is substantially similar to that of Pt (Table 2). E_{pp} is also directly responsible for the comparable electrocatalytic activities of the three CEs; moreover, this parameter is accounted for the similar overpotential loss of FeS$_2$, FeSe$_2$, and Pt-CE in DSCs. High peak current densities and similar E_{pp} of FeS$_2$ and FeSe$_2$ electrodes suggest that FeS$_2$ and FeSe$_2$ promote the high reversibility of I$_3^-$/I$^-$ redox reaction and remarkable electrocatalytic activity of I$_3^-$ reduction; this characteristic is a prerequisite for an excellent CE material in DSCs. Furthermore, FeTe$_2$ CE yields a high E_{pp} (199 mV), which indicates that the electrocatalytic activity of FeTe$_2$ CE is slightly inferior to that of FeS$_2$ and FeSe$_2$ electrodes. The electrochemical stability of a CE is of great importance in terms of additional DSC applications. We measured the sequential CVs for 120 cycles by using three iron chalcogenide electrodes, and the result is shown in Figure S3. A slight variation was observed in current density; therefore, these iron chalcogenide CEs exhibit good stability.

EIS is a powerful electrochemical method to characterize intrinsic interfacial charge transfer and charge transport kinetics at an electrode/electrolyte interface. We conducted EIS measurements by using symmetrical FeS$_2$/FeS$_2$, FeSe$_2$/FeSe$_2$, FeTe$_2$/FeTe$_2$, and Pt/Pt electrochemical cells under dark conditions; we then investigated the charge transfer at the electrode/electrolyte interface. The obtained Nyquist plots of the four CEs are presented in Figure 7; two semicircles can be observed at high- (left) and low-frequency (right) regions. The results were then fitted using Z-view software, and the equivalent circuit diagram shown in the inset in Figure 7a. The relevant EIS parameters of the four symmetrical cells are summarized in Table 2. Ingeneral, a high-frequency intercept on the real axis represents series resistance (R_s), which is mainly composed of the bulk resistance of CE materials, the resistance of the FTO substrate, and the contact resistance, among others. The left semicircle at the high-frequency range corresponds to the charge transfer resistance (R_{ct}) at the CE/electrolyte interface involved in I$_3^-$ reduction; the corresponding constant phase angle element indicates the deviation from ideal capacitance because of electrode roughness. The right semicircle at the low-frequency range corresponds to Nernst diffusion impedance (Z_N) of I$_3^-$/I$^-$ redox species transport in the electrolyte. In Table 2, R_s values of FeS$_2$, FeSe$_2$, FeTe$_2$, and Pt CEs were 8.91, 8.65, 7.51, and 8.27Ωcm^2, respectively, which may be related to electrode conductivity.
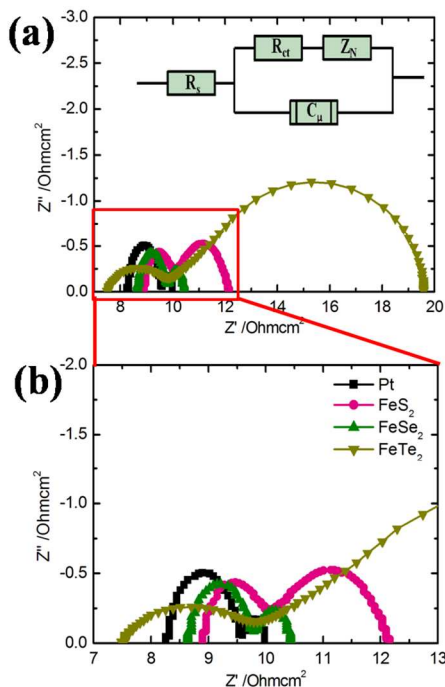
Figure 7. (a)Nyquist plots of the symmetrical cells fabricated with two identical CEs in the I_3^-/I^- electrolyte system. (b) Magnified Nyquist plotsof the square frame in (a). The measured frequencies range from 1 MHz to 100 mHz, and the spectra were obtained in the same redox active electrolyte at the same bias potential (–0.75 V).

FeTe$_2$ CE yielded the smallest R_s, which may be attributed to a relatively higher electrical conductivity; this result is consistent with that of previous theoretical calculation. R_s can be improved by optimizing fabrication conditions to significantly enhance the photovoltaic performance of DSCs.[49] R_{ct} of symmetric cells based on FeS$_2$, FeSe$_2$, FeTe$_2$, and Pt CEs are 0.44, 0.55, 1.08, and 0.64Ωcm^2, respectively. This finding indicated that the three chalcogenide CEs exhibited a high catalytic activity implicated in I_3^- reduction in DSCs and may also be attributed to high intrinsic catalytic activity. FeTe$_2$ CE presented a higher Z_N than Pt CE; this higher Z_N may be the main factor causing a relatively low electrocatalytic activity.[37] Furthermore, the higher Z_N of FeTe$_2$ may be caused by larger particales, resulting in a decrease in the number of catalytic active sites and a slightly inferior catalytic activity. Indeed, the conclusions derived from EIS and CV data are consistent. Moreover, FeS$_2$ and FeSe$_2$ CEs can compete with Pt CE in DSCs applications.

Tafel polarization tests were conducted to further elucidate the interfacial charge transfer properties of the I_3^-/I^- redox shuttle on an electrode surface. Figure 8 shows the Tafel polarization curves of the symmetrical cells based on FeS$_2$, FeSe$_2$, FeTe$_2$, and Pt CEs. In theory, a Tafel curve is composed of three zones: polarization zone represented by a curve at low potentials ($|V| < 120$ mV); a Tafel zone represented by a curve at moderate potentials (with a sharp slope); and a diffusion zone represented by a curve at high potentials (horizontal part). In the Tafel zone, the intersection of a cathodic branch and an equilibrium potential line can be regarded as exchange current density (J_0), which can be obtained by extending the line to
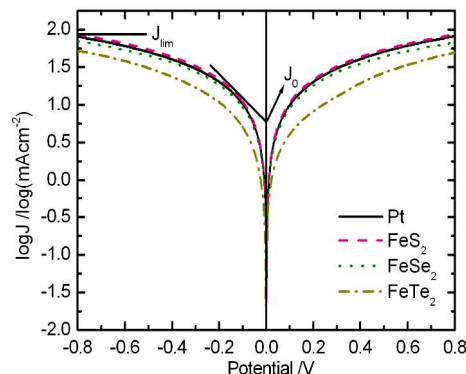
Figure 8. Tafel polarization curves of the symmetrical cells based on the various electrodes.

zero voltage and by measuring the intercept on the y-axis. A steep gradient of the Tafel zone corresponds to a high J_0 to some degree. The cathodic branches of the Tafel curves of FeS$_2$ and FeSe$_2$ CEs display larger slopes than those of Pt-CE and FeTe$_2$ CE (Figure 8); this result suggests that high J_0 is generated from FeS$_2$ and FeSe$_2$ electrodes. This result also indicates that FeS$_2$ and FeSe$_2$ electrodes can trigger the reduction of I_3^- to I^- as effectively as Pt CE. In theory, J_0 changes inversely with R_{ct}, which is consistent with EIS values, as expressed in Equation (5), where R is the gas constant, T is the temperature, F is Faraday's constant, n is the number of electrons exchanged in the reaction at the electrolyte/CE interface, and R_{ct} is the charge transfer resistance.

$$J_0 = \frac{RT}{nFR_{ct}} \tag{5}$$

In the diffusion zone, the intersection of the cathodic branch with the y-axis shows the limiting diffusion current density (J_{lim}), which is determined on the basis of the diffusion properties of a redox couple and CE catalysts, as expressed in Eq (6), where D is the diffusion coefficient, l is the spacer thickness, and c is the I_3^- concentration. A high J_{lim} indicates a large diffusion coefficient and a small Z_N at the same potential. FeS$_2$ CE yields J_{lim} similar to Pt CE. By contrast, FeSe$_2$ CE shows a slightly low J_{lim}; this result suggests a high diffusion velocity of I_3^- in the electrolyte, thereby causing a relatively higher photovoltaic performance when FeSe$_2$ is used as CE. FeTe$_2$ CE exhibited moderate J_{lim} values.

$$D = \frac{l}{2nFc}J_{lim} \tag{6}$$

Based on these theoretical and experimental results of the comprehensive analysis of the electrocatalytic activity of CEs for the I_3^-/I^- redox couple, our conclusion is that the three iron chalcogenides showed excellent catalytic activity for the I_3^- reduction; these chalcogenides are very suitable as CE materials of DSCs. FeTe$_2$ presents a slightly inferior catalytic activity possibly attributed to the larger particles than other CEs. Therefore, the catalytic activity of FeTe$_2$ can be improved through the regulation of morphological characteristics.

4.4 Photovoltaic performance of DSCs

To demonstrate the catalytic activity of the three chalcogenide CEs characterized by theoretical and experimental methods, we assembled DSCs with FeS$_2$, FeSe$_2$, and FeTe$_2$ CEs; we then
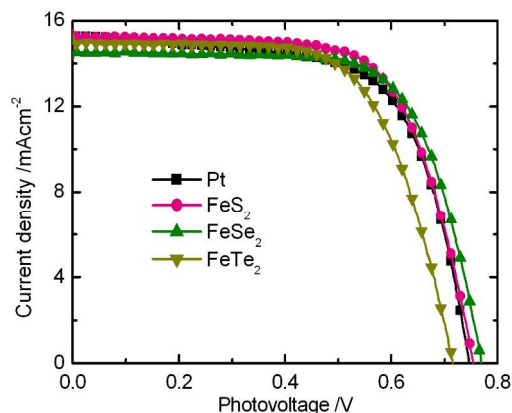
Figure9. Photocurrent–voltage (*J-V*) curves of DSCs based on the three chalcogenides and Pt CEs determined under simulated sunlight illumination conditions (Xe arc lamp, 1.5 AM, 100 mW· cm^{-2}).

investigated the photocurrent–voltage (*J–V*) curves (Figure 9). Table 2 summarized the corresponding photovoltaic parameters. The DSCs based on FeS$_2$ CE exhibited a short-circuit photocurrent (J_{SC}) of 15.55 mAcm^{-2}, an open-circuit voltage (V_{OC}) of 753 mV, a fill factor (*FF*) of 0.68, and a power conversion efficiency (*PCE*) of 8.00%. The DSCs based onFeSe$_2$ CE yielded J_{sc} of 14.23 mA·cm^{-2}, V_{oc} of 769 mV, *FF* of 0.72, and *PCE* of 7.92%. The DSCs based on sputtering Pt CE displayed J_{SC} of 15.28 mA·cm^{-2}, V_{OC} of 747mV, *FF* of 0.67, and *PCE* of 7.70%. Therefore, FeS$_2$- or FeSe$_2$-based DSCs showed a comparable (even slightly higher) *PCE* to sputtering Pt-based DSCs; this finding can be mainly attributed to the slight improvement in J_{sc} and *FF* of the DSCs with FeS$_2$ CE and in V_{OC} and *FF* of the DSCs with FeSe$_2$. FF may be improved because of a relatively small impedance of chalcogenides CE; these finding are consistent with those of EIS experiments. The DSCs based on FeTe$_2$ CE exhibited lower V_{OC} and *FF* than those based on other CEs; *PCE* of 7.21% was obtained. The relatively higher V_{OC} reflects the higher eletrocatalytic activity of FeS$_2$ and FeSe$_2$ CEs, which shifted the redox potential of I$_3^-$/I$^-$ to the positive direction.[50] FeS$_2$ and FeTe$_2$ showed relatively higher J_{SC}, which could be derived from an excellent catalytic activity of FeS$_2$ and good electrical conductivity for FeTe$_2$. By contrast, FeSe$_2$ yielded a relatively small J_{SC}, which could be related to the nanorod structure. Indeed, FeTe$_2$ CE shows a good electrocatalytic activity in I$_3^-$ reduction. A slightly lower *PCE* of the FeTe$_2$-based DSCs may be caused by the larger particles of this material; as a result, the number of catalytic active sites is decreased. Therefore, the catalytic activity of FeTe$_2$ can be improved by adjusting morphological characteristics.

4. Conclusions

In summary, the electrolytic behaviors of FeS$_2$, FeSe$_2$, and FeTe$_2$ on the reduction of I$_3^-$ in DSCs were systematically investigated using theoretical and experimental methods. Combining the calculated results of adsorption energy and work function, we suggest that the three iron chalcogenides showed excellent catalytic activities for I$_3^-$ reduction. A very strong hybridization among I *p* orbital, Fe *d* orbital and chalcogen *p* orbital indicated a strong interaction among these elements. Electrochemical experimental results demonstrated that pyrite FeS$_2$ nanoparticles, orthorhombic FeSe$_2$ nanorods, and orthorhombic FeTe$_2$ micron bulks showed superior electrolytic activities. The DSCs with iron chalcogenides CEs exhibited photovoltaic performances comparable to the DSCs based on Pt CE. Our findings further indicated that iron chalcogenides displayed excellent electrocatalytic activities. This study also provided a method to rationally screen cost-effective and highly efficient catalytic materials for electrocatalysis applications.

Notes and references

[a] State Key laboratory of Fine Chemicals, School of Chemistry, Dalian University of Technology, Dalian, 116024, P. R. China.
E-mail: tinglima@dlut.edu.cn; shiyantao@dlut.edu.cn
[b]College of Chemistry and Materials Engineering, Anhui Science and Technology University, Fengyang, Anhui, 233100, P. R. China.
[c]School Petroleum and Chemical Engineering, Dalian University of Technology, Panjin Campus, Panjin 124221, P. R. China
[d]Graduate School of Life Science and Systems Engineering Kyushu Institute of Technology, Kitakyushu, Fukuoka, 808-0196, Japan
† Electronic Supplementary Information (ESI) available: Theoretical lattice constants. XRD and SEM of FeTe$_2$ with different reaction times; Consecutive CVs of three iron chalcogenides CEs; See DOI: 10.1039/b000000x/
‡ JiahaoGuo and Suxia Liang contributed equally to this work.

1   G. Q. Zhang, B. Y. Xia, X. Wang, X. W. (David) Lou, *Adv. Mater.,* 2014,**26**, 2408.

2   M. Grätzel, *Nature,*2001, **414**, 338.

3   F. Gao, Y. Wang, D. Shi, J. Zhang, M. Wang, X. Jing, R. Humphry-Baker, P. Wang, S. M. Zakeeruddin, M. Grätzel, *J. Am. Chem. Soc.,*2008, **130**, 10720.

4   AswaniYella, C. L. Mai, Shaik M. Zakeeruddin, S. N. Chang, C. H. Hsieh, C. Y.Yeh, M.Grätzel, *Angew. Chem.,* 2014,**126**,3017.

5   Brian O'Regan, M. Grätzel, *Nature*, 1991, **353**, 737.

6   Papageorgiou, N. Coord. *Chem. Rev.*, 2004, **248**,1421.

7   M.Wang, A. M.Anghel, B.Marsan, N.C.Ha, N. Pootrakulchote, S.Zakeeruddin, M.Grätzel, *J. Am. Chem. Soc.,*2009, **131**, 15976.

8   M. X. Wu, X. Lin, A. Hagfeldt, T. L. Ma, *Angew.Chem. Int. Ed.,*2011, **50**, 3520.

9   S. N. Yun, M. X. Wu, Y. D. Wang, J. Shi, X. Lin, A. Hagfeldt, T.L. Ma, *ChemSusChem,* 2013, **6**,411.

10 X. Zhang, X. Chen, S. Dong, Z. Liu, X. Zhou, J. Yao, S. Pang, H. Xu, Z. Zhang, L. Li, G. Cui, *J. Mater. Chem.A,*2013, **1**, 6067.

RSC Advances Accepted Manuscript

11 Q. W. Jiang, G. R. Li, X. P. Gao, *Chem. Commum.*, 2009,**45**, 6720.

12 G. Li, J. Song, G. Pan, X. Gao, *Energy Environ. Sci.,*2011, **4**, 1680.

13 G.H. Guai, M.Y. Leiw, C.M. Ng, C.M. Li, *Adv. Energy Mater.*, 2012, **2**, 334.

14 H. W. Zhou, Y. T. Shi, Q. S. Dong, Y. X. Wang, C. Zhu, L. Wang, N. Wang, Y. Wei, S. Y. Tao, T. L. Ma, *J. Mater. Chem.A,* 2014, **2**, 4347.

15 Y. Dou, G. Li, X. Gao, *Phys. Chem. Chem. Phys.,*2012, **14**, 1339.

16 S.H. Chang, M. D. Lu, Y. L. Tung, H.Y. Tuan, *ACS Nano,*2013, **7**, 9443.

17 C. W. Kung, H. W. Chen, C. Y. Lin, K. C. Huang, R. Vittal, K.C. Ho, *ACS Nano,*2012, **6**, 7016.

18 H. Sun, D. Qin, S. Huang, X. Guo, D. Li, Y. Luo, Q. Meng, *Energy Environ. Sci.,*2011, **4**, 2630.

19 J. H. Guo, Y. T. Shi, Y. T. Chu, T. L. Ma, *Chem. Commun.,*2013,**49**, 10157.

20 F. Gong, H. Wang, X. Xu, G. Zhou, Z. S. Wang, *J. Am. Chem. Soc.*, 2012, **134**, 10953.

21 F. Gong, X. Xu, Z. Q. Li, G. Zhou, Z. S. Wang, *Chem. Commun.*, 2013, **49**, 1437.

22 J. H. Guo,Y. T. Shi, C. Zhu, L. Wang, N. Wang, T. L. Ma, *J. Mater.Chem.A,*2013, **1**, 11874.

23 J. M. Yan, H. Z. Huang, J. Zhang, Z. J. Liu, Y. Yang, *J. Power sources,*2005,**146**, 264.

24 R. Z. Yang, Z. X. Wang, J. Y. Liu, L. Q. Chen, *Electrochem. Solid-SatateLett.,*2004,**7**, A496.

25 M. Nath, A. Choudhury, A. Kundu, C.N.R. Rao, *Adv. Mater.,* 2003,**15**, 2098.

26 M. Nath, C.N.R. Rao, *Angew. Chem., Int. Ed.,*2002,**41**, 3451.

27 K.B. Tang, Y.T. Qian, J.H. Zeng, X.G. Yang, *Adv. Mater.,*2003,**15**, 448.

28 M. Bruchez, M. Moronne, P. Gin, S. Weiss, A. P. Alivisatos, *Science,*1998,**281**, 2013.

29 C. Ma, Y. Ding, D. Moore, X. Wang, Z. L. Wang, *J. Am. Chem. Soc.,* 2004,**126**, 708.

30 Y. Yang, X. J. Fan, G. Casillas, Z. W. Peng, G. D.Ruan, G. Wang, M. J.Yacaman, James M. Tour, *ACS Nano,*2014,**8**,3939.

31 J. X. Li, M. Z. Zou, L. Z. Chen, Z. G. Huang, L. H. Guan, *J. Mater. Chem.A*, 2014, **2**, 10634.

32 J. S. Lee, G. S. Park, S. T. Kim, M. L. Liu, J. Cho, *.Angew. Chem.,*2013, **125**, 1060.

33   Z. H. Wen, S. Q. Ci, F. Zhang, X. L. Feng, S. M. Cui, S. Mao, S. L. Luo, Z.He, J. H. Chen, *Adv. Mater.,*2012, **24**, 1399.

34 Y. C. Wang, D. Y. Wang, Y. T. Jiang, H. A. Chen, C. C. Chen, K. C.Ho, H. L. Chou, C. W. Chen, *Angew. Chem.,*2013, **125**, 6826.

35 Y. Hou, D. Wang, X. H. Yang, W. Q. Fang, B. Zhang, H. F. Wang, G. Z. Lu, P. Hu, H. J. Zhao, H. G. Yang, *Nature Commun.,* 2013,**4**, 1583.

36 L. Wang, Y. T. Shi, Y. X. Wang, H. Zhang, H. W. Zhou, Y. Wei, S. Y. Tao, T. L. Ma, *Chem. Commun.*, 2014, **50**, 1701.

37 L. Wang, Y. T. Shi, H. Zhang, X. G. Bai, Y. X. Wang, T. L. Ma, *J. Mater. Chem.A*, 2014, **2**, 15279.

38 G.Kresse, & J. Hafner, *Phys. Rev. B.*, 1994,**49**,14251.

39 G.Kresse, & J.Furthmuller, *Comput. Mater. Sci.*, 1996,**6**,15.

40 G. Kresse, & J. Furthmuller, *Phys. Rev. B,*1996,**54**,11169.

41 P. E.Blöchl, *Phys. Rev. B,*1994,**50**,17953.

42 X. Fang, T. Ma, M. Akiyama, G. Guan, S. Tsunematsu, E. Abe,*Thin Solid Films*, 2005, **472**, 242.

43 M. X. Wu, X. Lin, T. H. Wang, J. S. Qiu, T. L. Ma, *Energy Environ. Sci.* 2011, **4**, 2308.

44 T. Harada, *J. Physical society of Japan*, 1998,**67**, 1352.

45 A. Hauch, A.Georg, *Electrochim. Acta*, 2001,**46**, 3457.

46 F. F. Volkenstein, The Electronic Theory of Catalysis on Semiconductors (Pergamon Press, Oxford, 1963).

47 B. X.Yuan, W. L.Luan and S. T.Tu,*Dalton Trans.*, 2012, **41**, 772.

48 W. X. Zhang, Z. H. Yang, J. H. Zhan, L. Yang, W. H. Yu,G. E. Zhou, Y. T. Qian, *Materials Letters*, 2001, 47, 367.

49 P. Joshi, L. Zhang, Q. Chen, D. Galipeau, H. Fongand Q. Qiao, *ACSAppl. Mater. Interfaces*, 2010, **2**,3572.

50 L. Yi, Y. Liu, N. Yang, Z. Tang, H. Zhao, G. Ma, Z. Sua andD. Wang, *Energy Environ. Sci.*, 2013, **6**, 835.

Electrocatalytic Properties of Iron Chalcogenides as Low-Cost Counter Electrode Materials for Dye-sensitized Solar Cells

Jiahao Guo,[a,b] Suxia Liang,[a] Yantao Shi,[a*] Ce Hao,[a] Xuchun Wang,[b] and Tingli Ma[a,c*]

[a] State Key laboratory of Fine Chemicals, School of Chemistry, Dalian University of Technology, Dalian, 116024, China. Fax: +86 0411 39893820; E-mail: tinglima@dlut.edu.cn; shiyantao@dlut.edu.cn
[b] College of Chemistry and Materials Engineering, Anhui Science and Technology University, Fengyang, Anhui, 233100, China.
[c] Graduate School of Life Science and Systems Engineering Kyushu Institute of Technolog 2-4 Hibikino, Wakamatsu, Kitakyushu, Fukuoka, 808-0196, Japan

Three iron chalcogenides, FeS_2, $FeSe_2$ and $FeTe_2$, were successfully prepared by different synthetic routes to conduct both experimental and theoretical investigations of iron chalcogenides as CE materials in DSCs, and meanwhile to probe the origin of their high electrocatalytic activity for I_3^- reduction. The devices using these three CEs obtained high photovoltaic conversion efficiencies (PCEs) of 8.00%, 7.92% and 7.21%, respectively, comparable to that of 7.70% based on the sputtering Pt CE. Experimental results were confirmed by theoretical calculations. The findings in this work may provide valuable information in understanding the electrocatalytic principle and thus offer some guidelines to develop more efficient inorganic electrocatalysts.